Seasonal bias in global observations of ocean color

K. M. Bisson[1], E. Boss[2], P. J. Werdell[3], A. Ibrahim[3,4], Robert Frouin[5], and M. J. Behrenfeld[1]

[1]Department of Botany and Plant Pathology, Oregon State University, Corvallis, Oregon, 97331, USA.

[2]School of Marine Sciences, University of Maine, Orono, Maine, 04469, USA.

[3]Ocean Ecology Laboratory, NASA Goddard Space Flight Center. Greenbelt, Maryland, 20771, USA.

[4]Science Systems and Applications Inc., Lanham, Maryland, 20706, USA.

[5]Scripps Institution of Oceanography, La Jolla, California, 92093, USA

Corresponding author: Kelsey Bisson (bissonk@oregonstate.edu)

Abstract (up to 400 words)

In this study we identify a global seasonal bias in ocean color remote sensing reflectances (R_{rs}, λ) using data from the CALIOP (Cloud-Aerosol Lidar with Orthogonal Polarization) instrument aboard the CALIPSO (Cloud-Aerosol Lidar and Infrared Pathfinder) satellite, in addition to Argo floats and in-water reflectance from the Marine Optical BuoY (MOBY) site. The seasonal bias in R_{rs} is present in the VIIRS (Visible Infrared Imaging Radiometer Suite), SeaWIFS (Sea-viewing Wide Field-of-view sensor), and MODIS (Moderate resolution imaging spectrometer) satellites at all visible wavelengths and is larger at longer wavelengths. Products derived from R_{rs} are affected by the bias to varying degrees, with particulate backscattering varying up to 50% over a year, chlorophyll varying up to 25% over a year, and absorption from phytoplankton or dissolved material varying by up to 15%. The seasonal bias is prominent in areas of low biomass (i.e., gyres) and is not easily discernable in areas of high biomass. We found that the seasonal bias in R_{rs} is not caused by Raman scattering choice or implementation, nor is it due to differences with satellite viewing angle. Biases in particulate backscattering are not affected by specific

assumptions used within R_{rs} inversion models. Changing the specific space/time averaging window in different processing levels of remote sensing data and matchups were not the cause either. While we have eliminated several candidates which could cause the bias, there are still outstanding questions about the role atmospheric correction plays. We provide evidence that the Bidirectional Reflectance Distribution Function correction factor may control the observed seasonal bias to some extent, but does not preclude the effect of the aerosol correction. We provide recommendations for work to be conducted in the near-future. In particular, the use of CALIOP aerosol data may help improve the aerosol model used in atmospheric correction and the execution of more simulations to discern the relative influence of atmospheric correction parameters. Community efforts are needed to find the root cause of the seasonal bias because all past, present, and future data will be affected until a solution is implemented.

1 Introduction

Remote sensing reflectance (R_{rs} (λ); sr^{-1}) is the fundamental measurement that links the marine environment to satellite observations. Since the launch of the Coastal Zone Color Scanner in 1978, satellite observations of R_{rs} and its derived products (chlorophyll; mg m^{-3}, particulate organic carbon; mg m^{-3}, particulate backscattering; λ, m^{-1}, particulate absorption; λ m^{-1}, phytoplankton absorption; λ, m^{-1}, dissolved organic matter; λ, m^{-1}) have been used to quantify global net primary production (Behrenfeld and Falkowski, 1997, Westberry et al., 2008), global carbon export and associated pathways for sinking (e.g., Siegel et al., 2014), particulate organic carbon (Stramski et al., 1999, Evers-King et al., 2017), phytoplankton size (Kostadinov et al,. 2010, Loisel et al., 2006) and community composition (Uitz et al., 2010, Bracher et al., 2009, Sathyendranath et al., 2014, Kramer et al., 2018, Lange et al., 2020), harmful algal blooms

(Dierssen et al., 2015, Wei et al., 2008, Stumpf, 2001), phytoplankton carbon and physiology (Behrenfeld et al., 2005, Behrenfeld et al., 2009), nitrogen fixation (Westberry and Siegel., 2006), river plumes and suspended sediments (Stumpf, 1988, Yu et al., 2019, Tao and Hill, 2019), dissolved organic matter (Hoge and Lyon, 2002, Matsuoka et al., 2017), general ecological dynamics (Dutkiewicz et al., 2020 and refs therein), and climate change (Henson et al., 2010, Behrenfeld et al., 2016, Dutkiewicz et al., 2019).

Accurate, low-uncertainty, unbiased satellite R_{rs} (λ) observations are critical to advance our understanding of the marine carbon cycle and to improve predictive power of ecological and climate models built from R_{rs} (λ) data, especially because so many products are derived from R_{rs} (λ). Recently we compared particulate backscattering (b_{bp}) derived from MODIS-Aqua (Moderate Resolution Imaging Spectrometer) reflectances with b_{bp} derived from the CALIOP (Cloud-Aerosol Lidar with Orthogonal Polarization) instrument aboard the CALIPSO (Cloud-Aerosol Lidar and Infrared Pathfinder) satellite (Bisson et al., 2021). We found that the CALIOP b_{bp} data clearly outperformed MODIS b_{bp}, both in terms of median percent error and bias. Regional variations in MODIS b_{bp} relative to CALIOP b_{bp} were large (in some places exceeding 50%), making it clear that further research is warranted.

In this paper, we perform a global evaluation of ocean color observations [including MODIS, SeaWiFS (Sea-viewing Wide Field-of-view sensor), and VIIRS (Visible Infrared Imaging Radiometer Suite)] using CALIOP and Argo float b_{bp} data. We find that ocean color R_{rs} is seasonally biased on global scales. A similar seasonal bias is also found when evaluated at the local scale of MOBY (Marine Optical BuoY) observations. We provide preliminary evidence that the bias arises from the bidirectional reflectance distribution function (BRDF) used to generate MODIS R_{rs}, combined with the aerosol correction residual effect. At the time of this

writing, no solution has been found to correct the seasonal bias. Ultimately, community input is needed to help correct the seasonal bias and advise atmospheric correction protocols for future satellite missions, such as PACE (Plankton, Aerosol, Cloud, ocean Ecosystem, (Werdell et al., 2019).

2.0 Methods

We acquired satellite data from MODIS, VIIRS, SeaWiFS, and CALIOP. We compared these data at different processing levels with regional and local data using either autonomous profiling floats from the Argo program or observations from MOBY. The overall goal was to diagnose the observed seasonal bias by comparing a range of satellite observations at different places and times.

2.1 Acquiring and processing ocean color data

All ocean color R_{rs} data were acquired from <oceancolor.gsfc.nasa.gov>. In particular, global level-3 9km daily MODIS and VIIRS R_{rs} (λ) data were downloaded over the time period 2008-2017, where CALIOP data were also available. Level-3 9km daily global SeaWiFS data were downloaded from 2008-2010 (the shared time period between SeaWiFS and CALIOP). We also downloaded 1-degree monthly averages of R_{rs} and b_{bp} (GIOP product) from the overall MODIS mission. Level-2 1km R_{rs} data were obtained in the South Pacific, Indian Ocean, and South Atlantic regions where there are also abundant Argo float observations over the seasonal cycle. These data were used to facilitate comparisons with CALIOP and MODIS on finer scales. Level-2 1km R_{rs} data also provided ancillary data regarding atmospheric aerosol optical

thickness (869 nm), solar zenith angle, photosynthetically active radiation (PAR), and the Angstrom parameter used in atmospheric correction schemes.

We retrieved level-2 MODIS R_{rs} paired with R_{rs} measured at the MOBY site from the NASA time series tool (https://seabass.gsfc.nasa.gov/timeseries/) and we calculated monthly averages of MOBY and MODIS R_{rs} at 412, 443, 531, 555, and 667 nm. For MODIS, MOBY, SeaWiFS, and VIIRS, b_{bp} is linked to R_{rs} through the semi-analytical relationship:

$$\frac{R_{rs}(\lambda)}{0.52+1.7R_{rs}(\lambda)} = G_1*[\frac{b_b(\lambda)}{a(\lambda)+b_b(\lambda)}]+G_2*[\frac{b_b(\lambda)}{a(\lambda)+b_b(\lambda)}]^2, \quad (1)$$

where the left side of the equation converts R_{rs} into its subsurface values (via Lee et al., 2002). On the right side of equation 1, $G_1 = 0.0949$ and $G_2 = 0.0794$ (Gordon et al. 1988), $b_b(\lambda)$ is total backscattering, and $a(\lambda)$ is total absorption (i.e., the sum of seawater absorption, absorption from colored dissolved organic matter, non-algal particles, and phytoplankton). Total backscattering is the sum of seawater backscattering (b_{bw}) and particulate backscattering (b_{bp}), which is approximated spectrally as an amplitude (M_{bp}) times a power-law function of wavelength (with exponent (γ):

$$b_b(\lambda) = b_{bw}(\lambda) + M_{bp}\lambda^{-\gamma}. \quad (2)$$

Although there are several inversion algorithms available to generate b_{bp} from R_{rs}, each with slightly different prescribed shapes for γ, we used the Generalized Inherent Optical Properties

algorithm in its default configuration (GIOP-DC, Werdell et al., 2013) because it has performed well in past work (Bisson et al., 2019) and because it is distributed through NASA's Ocean Biology Processing Group for community use. GIOP-DC allows the user to choose various parameterizations for either absorption or scattering. These various parameterizations account for different assumptions regarding relationships between R_{rs}, absorption, and scattering (Werdell et al., 2013).

R_{rs} needs to be corrected for the contribution of Raman scattering because b_{bp} can otherwise have errors up to ~50% (Westberry et al., 2013). We note that the currently distributed b_{bp} and absorption products through NASA's ocean color website have not been Raman corrected (future processing will include Raman-corrected products). Here, we have considered 3 options for treating the Raman issue: 1) no Raman correction, 2) correction following the empirical approach of Lee et al., (2013), and 3) correction following the Westberry et al., (2013) scheme that merges OMI (ozone mapping instrument) and MODIS data to more comprehensively assess Raman excitation in the full visible spectrum. Spectral ultraviolet data from the OMI sensor were retrieved and averaged monthly at four fixed wavelengths (305, 310, 324, and 380 nm) from the Goddard Earth Sciences Data and Information Services Center (GES DISC). The Westberry et al., (2013) Raman scattering correction scheme also requires monthly averages of instantaneous photosynthetically active radiation (iPAR), which were acquired from <oceancolor.gsfc.nasa.gov>. Unless specified otherwise, R_{rs} products were corrected for Raman scattering following the Lee et al., (2013) scheme.

2.2 CALIOP b_{bp}

CALIOP is a light detection and ranging (lidar) instrument aboard the CALIPSO satellite that was launched with the intention of improving cloud and aerosol characterization. Like MODIS, CALIOP flies in the A-train constellation, but unlike MODIS, CALIOP was not launched with oceanographic research in mind. However, CALIOP data have since been used to generate b_{bp} at 532 nm using polarization properties of this nadir-viewing lidar (see details in Behrenfeld et al., 2013). CALIOP provides a repeated global sampling of the oceans and retrieves independent assessments of the particulate backscattering coefficient (b_{bp}, m^{-1}). Ocean color satellites likewise retrieve b_{bp} from R_{rs}, so it is possible to compare CALIOP b_{bp} (532 nm) with $b_{bp}(\lambda)$ derived from MODIS-Aqua (Moderate Resolution Imaging Spectrometer) $R_{rs}(\lambda)$ over their shared time period where data are available (2008-2017).

We acquired daily CALIOP b_{bp} data over the time period 2008-2017 from the Oregon State University Ocean Productivity website (http://orca.science.oregonstate.edu/lidar_nature_2019.php). A scattering phase function of 0.32 was used in calculating b_{bp} from CALIOP observations, following Lu et al. (2020), Lacour et al. (2020), and Bisson et al. (2021). All CALIOP daily data were binned into monthly 9km grids for comparison with MODIS data. We also compared monthly averaged CALIOP and MODIS data binned to 1-degree grids.

2.3 Argo float b_{bp}

We used Argo data in this study because Argo floats provide independent in-situ measurements of b_{bp} worldwide that are a useful asset with which to confront CALIOP and MODIS data. Vertical profiles of b_{bp} (700 nm) from Argo floats were downloaded from the Argo Data Assembly Centre (ftp://ftp.ifremer.fr/ifremer/argo/dac/ on 20 May, 2020) and processed as

in Bisson et al. (2019). In particular, vertical profiles of b_{bp} were de-spiked with a 3-pt moving median and the reported b_{bp} values were the median b_{bp} value within the mixed layer depth (where density exceeded 0.03 kg m^{-3} compared to the density at 10m) of every profile. Previous work compared point-by-point matchups between Argo, MODIS, and CALIOP and found that CALIOP outperformed MODIS with respect to b_{bp} retrievals [where median percent errors were 25% for MODIS and 16% for CALIOP (Bisson et al., 2021)]. Here, rather than point-by-point comparisons, we compared the seasonal cycle of Argo b_{bp} with MODIS and CALIOP. Because there are insufficient measurements of Argo b_{bp} for any given month, we calculated monthly averages over the entirety of Argo sampling for specific regions. We extrapolated Argo b_{bp} to 531 nm for comparison with MODIS using b_{bp} spectral slopes derived from collocated MODIS R_{rs} (λ).

2.4 Multivariate regression analysis on MOBY and MODIS data

Multivariate regression analysis (MLR) provides insight into the dependence of the R_{rs} matchups on other supposedly independent variables that are accounted for in the atmospheric correction. The atmospheric correction removes the radiometric effect of the atmosphere from the satellite observations by removing the air molecule and aerosol absorption and scattering, removing the ocean surface glint and white caps, and applying the BRDF to get the R_{rs} (Mobley et al, 2016). We utilized a probabilistic programming Python library, PyMC3, which allows us to infer a posterior distribution from observed data and a prior probability (Salvatier et al, 2016). Using the MLR analysis, we modeled MODIS Aqua R_{rs} ($Rrs_{¿}$, derived from satellite data after the atmospheric correction) as a function of all other variables, including MOBY R_{rs} (Rrs_{moby}¿, BRDF correction factor ($f_{brdf}(\lambda)$), windspeed (W_s), glint coefficient (L_{GN}), column water vapor (

185 Cwv), column ozone (O_3), pressure (Pr), relative humidity (Rh), angstrom coefficient (α_a),
186 aerosol optical depth (τ_a), and solar zenith (θ_{sol}), sensor zenith (θ_{sen}), and relative azimuth (φ)
187 angles. The $Rrs_{¿}$ model is assumed to follow a Student's t distribution rather than a normal
188 distribution because in situ matchups rarely follow a normal distribution and because Student's t
189 allows for additional degrees of freedom to compensate for strong outliers. This assumption is
190 in-effect similar to the outliers filtering procedure used in the vicarious calibration process at
191 MOBY by excluding points outside the inter-quantile range (Franz et al, 2007). $Rrs_{¿}$ is modeled
192 as follows:
193
194 $Rrs_{¿}\ \ St(\mu, v)$, [3]
195
196 where μ, and v are the mean, and degree of freedom of the Student's t distribution, respectively,
197 and μ is modeled as:
198
199 $$\mu = \beta_0 Rrs_{moby} + \beta_1 \theta_{sol} + \beta_2 \theta_{sen} + \beta_3 \varphi + \beta_4 W_s + \beta_5 L_{GN} + \beta_6 Cwv + \beta_7 Rh + \beta_8 O_3 + \beta_9 Pr + \beta_{10} \alpha_a + \beta_{11} \tau_a + \beta_{12} f_{brdf} + \alpha$$
200 . [4]
201
202 Slope coefficients of each independent variable are given in [4] by β_i, where α is the intercept.
203 The prior distribution of β_i and α are assumed weakly informative with mean of zero and a
204 standard deviation of 100. Since the magnitude and the dynamic range of each variable is
205 different, we scaled the data by subtracting the mean and dividing by the standard deviation of
206 each variable (thus all the data have a mean of zero and a standard deviation of one). The
207 intercept bias (α) then becomes zero. In this manner, the magnitude of the slopes become more

meaningful, such that one unit of change of the dependent variable is equivalent to one unit of change of the independent variables when a specific β_i is 1 (which means a 1-to-1 correspondence between the two variables).

3.0 Results

The primary result of a seasonal bias in MODIS b_{bp} (and R_{rs}) on scales spanning from local to global is highlighted in Figure 1, where a red band highlights higher MODIS: CALIOP b_{bp} ratio depending on the month (also see animation in Supplementary Figure 1). The Southern Ocean and the oligotrophic gyres in particular are places where the ratio of MODIS: CALIOP b_{bp} changes dramatically throughout the seasonal cycle.

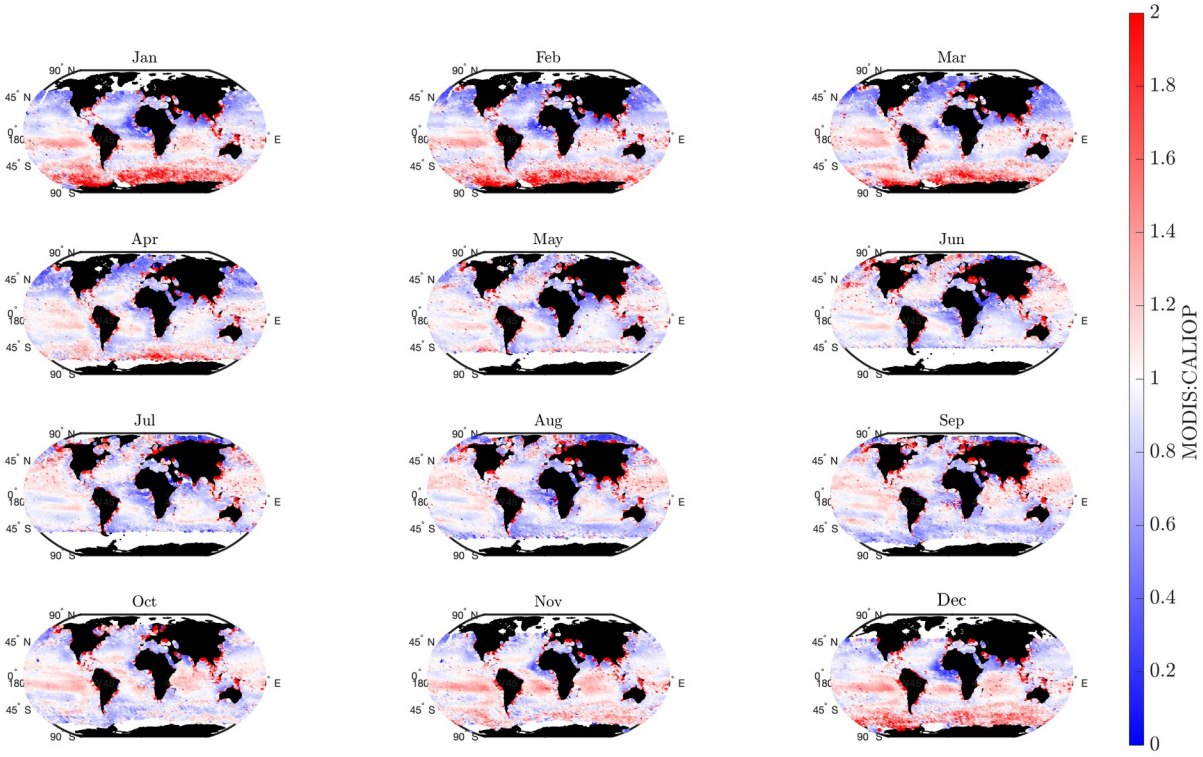

Figure 1. Monthly MODIS: CALIOP b_{bp} at 532 nm. MODIS and CALIOP b_{bp} are binned to 1-degree monthly averaged grids.

221

222 3.1 Bias diagnostic tests

223 The observed bias between CALIOP and MODIS b_{bp} (Figure 1) prompted a series of
224 diagnostic steps to uncover the root cause (Table 1), largely aimed at answering whether MODIS
225 or CALIOP provided the most robust b_{bp} record and diagnosing what causes the relative bias
226 between sensors. Because the magnitude of the b_{bp} bias varies by season across latitudinal bands,
227 we considered processing steps that may be affected by solar geometry and associated variables.
228 We asked a series of guiding questions and performed analysis to answer them:

229

230 1. What effect does Raman scattering have on the seasonal bias?

231 The relative importance of Raman scattering correction increases with increasing
232 wavelengths and solar irradiance and it decreases with increasing biomass. Solar irradiance and
233 biomass are seasonally variable, so it is plausible that Raman scattering could account for the
234 observed seasonal bias. Longer wavelengths (~530-700) already have high uncertainty due to
235 suboptimal signal to noise ratios and these longer wavelengths are used in inversion algorithms.
236 Previous work (Westberry et al., 2013) found a bias between Raman-corrected R_{rs} and
237 uncorrected R_{rs} that resulted in associated b_{bp} differences up to 50%. The regions most affected
238 by Raman scattering corrections were those with low biomass, such as the oligotrophic gyres
239 (Figure 8 in Westberry et al., 2013). Variations in R_{rs} (667 nm) throughout the annual cycle may
240 generate different quantities of Raman corrections based on season. We tested two different
241 Raman correction schemes for MODIS R_{rs} and we tested uncorrected MODIS R_{rs}. We also tested
242 different wavelengths of b_{bp} to see if the seasonal bias is more pronounced at longer wavelengths
243 (Supplementary Figure 1). The presence of the seasonal bias in b_{bp} was largely unaffected by

Raman choice or implementation (Supplementary Figure 2). However, the magnitude of the seasonal bias in b_{bp} is enhanced when a Raman scattering correction is not applied (Supplementary Figure 2a-c).

2. Is the seasonal bias in b_{bp} affected by parameterizations within the GIOP?

We tested alternative parameterizations within the GIOP because the retrieval of b_{bp} from ocean color is dependent on other assumptions within the inversion algorithm. In particular, absorption from phytoplankton and dissolved organic detrital matter will have different magnitudes depending on the season. Some parameterizations within the GIOP account for seasonality (e.g. changing spectral shape with biomass) and it is also possible to parameterize absorption or scattering constituents with a constant spectral shape that does not change based on place or time. For example, choosing a constant power-law exponent for b_{bp} spectral slope (as in Maritorena et al., 2002) will not change seasonally, while a b_{bp} slope derived from R_{rs} band ratios (as in Lee et al., 2013) will vary with the changing seasons. We altered the assumed spectral shape of absorption by phytoplankton (a_{ph}) and dissolved organic detrital material (a_{dg}), as well as the b_{bp} spectral exponent (Supplementary Figure 3). We found that the seasonal bias in MODIS and CALIOP b_{bp} is largely unaffected by changes to b_{bp}, a_{ph}, and a_{dg} parameterizations in GIOP.

3. Does R_{rs} processing level influence the seasonal bias in b_{bp}?

Different processing levels of R_{rs} reflect averaging of ocean color scenes over varied temporal windows. For example, at higher latitudes there can be multiple passes in a day at a particular location. Accordingly, a single 'daily' R_{rs} file may actually be a composite of various scenes from variable solar zenith angles. Thus, over the course of a season, the averaging of R_{rs}

267 into different products may be a potential source of the seasonal bias. We tested MODIS daily
268 level-3 9km data for exact matchups with CALIOP, and monthly climatology data for comparing
269 patterns between the annual cycles of CALIOP and MODIS (Supplementary Figure 4) for all
270 available data. We also tested MODIS level-2 1km imagery at particular regions to confirm that
271 the bias existed at the lowest available R_{rs} processing level. We did not find any substantial
272 differences in the bias based on processing level (Supplementary Figure 4).
273

274 4. Do VIIRS and SeaWiFS b_{bp} have a bias with CALIOP b_{bp}?

275 Looking into other (than MODIS) passive sensors was prompted by the idea that the
276 satellite viewing geometry may be the cause of the apparent seasonal bias. MODIS and CALIOP
277 are most sensitive to different scattering angles (MODIS: centered on 131º to 180º,
278 https://aqua.nasa.gov/modis and CALIOP: 180º), so there could be differences in b_{bp} solely
279 because each sensor views a different part of the volume scattering function. Sensor differences
280 when compared to CALIOP b_{bp} may also arise from sensor specific calibrations. We therefore
281 extended our analysis to include SeaWiFS and VIIRS data (Supplementary Figure 5). SeaWiFS
282 and VIIRS have different viewing angles compared to MODIS, so we hypothesized that the
283 magnitude of the bias may be affected by satellite viewing angle. Note that the passive satellite
284 viewing angles change with season as the sun angle changes, potentially creating a seasonal
285 trend. We found a similar seasonal bias in SeaWiFS and VIIRS data when compared to CALIOP
286 data (Supplementary Figure 5), implying that neither satellite viewing geometry nor sensor
287 specific calibrations are a fundamental reason for the observed seasonal bias in $R_{rs}(\lambda)$.
288

289 **Table 1**. Table of hypotheses used to diagnose the seasonal bias in initial observations of
290 MODIS and CALIOP b_{bp}.

Hypothesis	Outcome	Evidence
The bias is a function of wavelength	No	Figure S1
The bias arises from Raman scattering choice or implementation	No	Figure S2
The bias is caused by inversion assumptions (i.e., a_{ph}, a_{dg}, b_{bp}).	No	Figure S3
The bias is a function of MODIS R_{rs} processing level.	No	Figure S4
The bias exists in SeaWiFS and VIIRS data.	No	Figure S5
The bias is regionally apparent over an annual cycle.	Yes	Figure 2
The bias is present at the MODIS calibration site, MOBY.	Yes	Figures 3, 4

291

292 To summarize, we found that the seasonal bias was not substantially affected by b_{bp}
293 wavelength choice (Supplementary Figure 1), or by which Raman scattering choice was used,
294 including if no Raman scattering correction was applied (Supplementary Figure 2). The global
295 seasonal bias in b_{bp} was also sustained through changes in inversion algorithm assumptions
296 (Supplementary Figure 3), as well as across R_{rs} processing levels [i.e., daily R_{rs} observations used
297 to compute daily b_{bp} compared to monthly climatologies of b_{bp} over the duration of the mission
298 (Supplementary Figure 4)]. Finally, the seasonal global bias in b_{bp} is not limited to MODIS, but
299 is also found in SeaWiFS and VIIRS b_{bp} data when compared to CALIOP b_{bp} (Supplementary
300 Figure S5). Given these findings, we proceeded to evaluate if the seasonal bias was present on
301 local and regional scales (section 3.2).
302
303 3.2 Seasonal bias in b_{bp} on regional scales
304 The observed global seasonal bias between MODIS and CALIOP b_{bp} (Figure 1) is
305 particularly pronounced between 20S and 20N. Within this region there were numerous Argo
306 floats equipped with backscattering sensors in the South Pacific, allowing monthly averages of
307 b_{bp} to be constructed from 455 independent observations. Comparisons of Argo, MODIS, and

CALIOP b_{bp} throughout an annual cycle in the South Pacific reveals a seasonal bias between MODIS and either Argo or CALIOP (Figure 2a). In particular, MODIS b_{bp} (red line in Figure 2a) is roughly parabolic across the annual cycle compared to CALIOP and Argo b_{bp}, which exhibit little seasonal change. The exaggerated seasonality in MODIS, relative to CALIOP, results in a ratio between MODIS and CALIOP over the annual cycle that resembles what is found on global scales for the average annual cycle. In particular, MODIS b_{bp} exceeds CALIOP b_{bp} in the Austral summer (by up to nearly 60%) relative to MODIS values in the Austral winter, which agree within 20% of CALIOP b_{bp} (Figure 2b). We note that both CALIOP and MODIS b_{bp} exceed Argo b_{bp} in our South Pacific bin. CALIOP consistently overestimates Argo b_{bp} by about 30% and MODIS overestimates Argo b_{bp} by 30-100%, depending on the time of year. Argo and CALIOP measurements exhibit a relatively constant b_{bp} throughout the year (as might be expected for the South Pacific Gyre, an area with little seasonal variability), whereas the symmetric seasonality pronounced in MODIS observations are difficult to reconcile with the biology of the region.

Solar zenith angle and photosynthetically active radiation (PAR) also exhibit a roughly parabolic shape with season that is symmetrical across the annual cycle, as expected (Figure 2c). Band ratios of R_{rs} are not greatly affected by the inclusion of Raman scattering (Figure 2d), but overall the ratio of R_{rs} (412 nm): R_{rs} (531 nm) is marked by a clear periodicity that is also present in the aerosol optical thickness (AOT, Figure 2e) and angstrom parameter used within the atmospheric correction scheme (Figure 2f). Broadly similar trends in the comparison of MODIS b_{bp} with Argo and CALIOP b_{bp} are present within the central gyre of the South Atlantic and Indian oceans (Supplementary Figures 6,7). For these regions, the summer months see a higher MODIS: CALIOP b_{bp} ratio compared to winter months.

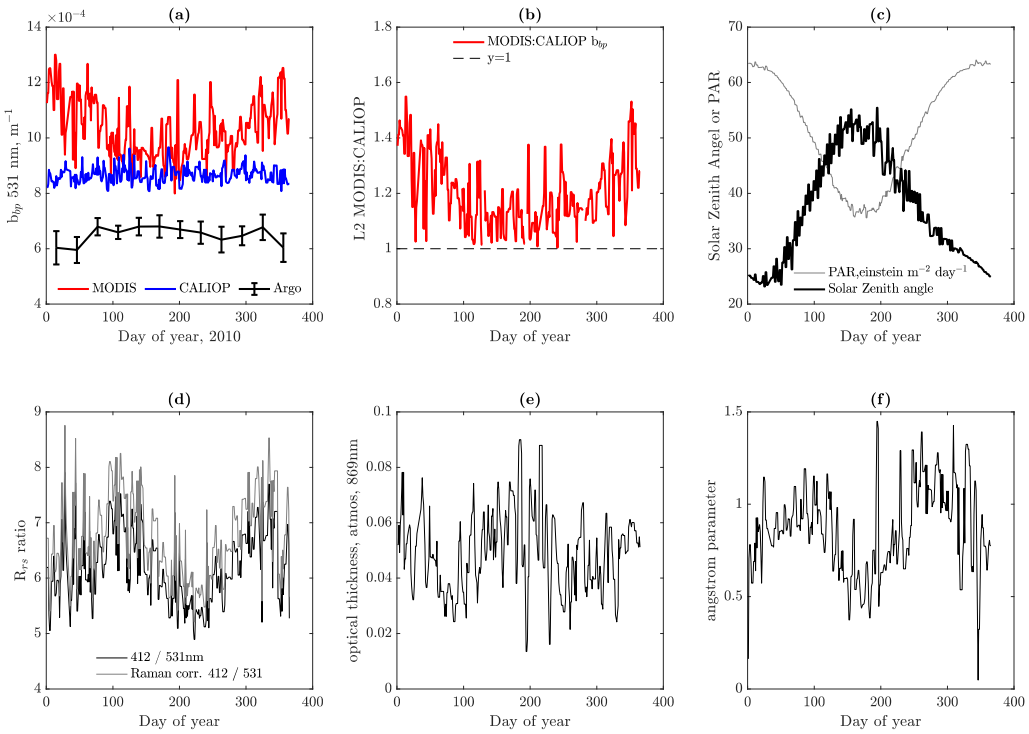

Figure 2. Comparison of MODIS Level-2 data with CALIOP b_{bp} and Argo b_{bp} in the South Pacific (20S, 110-165W). Note that MODIS and CALIOP data are for 2010, while the Argo data are monthly averages for 2016 to present (due to insufficient data within any given year). a) $b_{bp,}$ 531 nm. b) Ratio of MODIS:CALIOP b_{bp} over the annual cycle of 2010. c) Photosynthetically Active Radiation (PAR) and solar zenith angle. d) R_{rs} ratios (shown for both Raman corrected following Lee et al., 2013 and without Raman correction). e) Aerosol optical thickness. f) Angstrom parameter.

3.3 The seasonal bias in b_{bp} and R_{rs} at MOBY

The Marine Optical BuoY (MOBY) is stationed off Lanai, Hawaii and collects water leaving radiance measurements that are used to compute R_{rs}, primarily for vicarious calibration

of satellites (Clark et al., 2003). Monthly averaged R_{rs} at various wavelengths between MODIS and MOBY exhibit discrepancies over the seasonal cycle (Figure 3). At shorter wavelengths (412 and 443 nm), discrepancies between MODIS (black line) and MOBY (red line) are slight (Figure 3a, b) and the general seasonal cycle is consistent between data sets. However, at longer wavelengths (531-667, Figure 3c-e), the seasonal cycle of MODIS R_{rs} is very different from that of MOBY. Differences between MODIS and MOBY are modest (< 20%) for R_{rs} observations between 412-555nm (Figure 3f-i), but at 667nm, the differences reach 40%. The biggest discrepancies between MODIS and MOBY R_{rs} are during the summer months for all wavelengths, but at R_{rs} (667 nm), there are also sizeable differences (20%) in December and January.

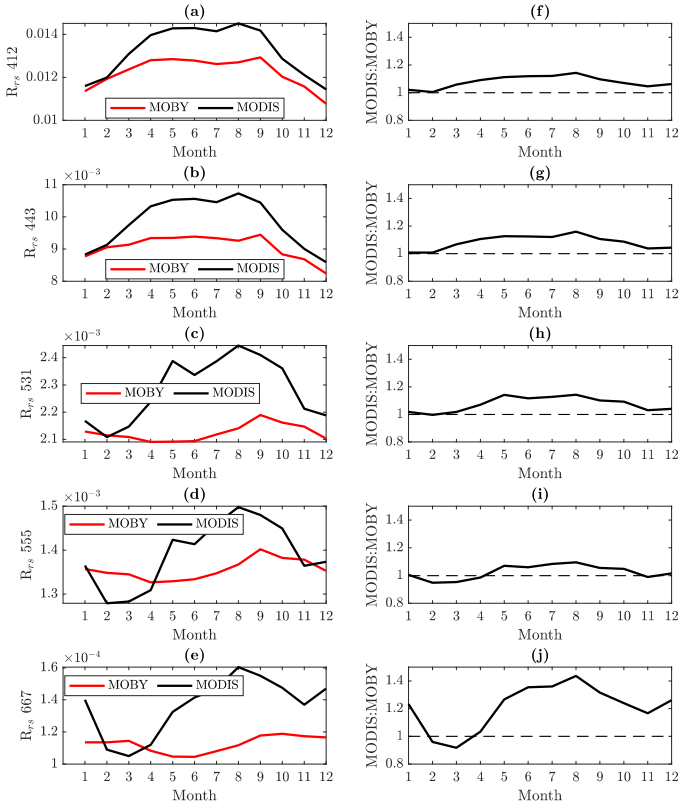

Figure 3. Left panel: Monthly averaged MODIS (black) and MOBY (red) R_{rs} at 412, 443, 531, 555, and 667 nm. Right panel: Corresponding MODIS: MOBY R_{rs} (black) relative to a ratio of 1 (dashed line) for all months of the year. Note that all possible MOBY and MODIS data are used (n = 6171 observations total) rather than limiting the analysis to just MODIS and MOBY matches.

When MOBY and MODIS R_{rs} are used to derive b_{bp}, the seasonal cycle observed between the two sensors is markedly different (Figure 4). MOBY (black dotted line) and CALIOP b_{bp} (blue solid line) exhibit weak seasonality at this location compared to MODIS (red line, Figure 4a). Moreover, MODIS: MOBY b_{bp} and MODIS:CALIOP b_{bp} have the same general shape over the annual cycle, suggesting that MOBY and CALIOP b_{bp} are more similar to each other than either one is to MODIS (Figure 4b). The seasonal bias between MODIS and CALIOP b_{bp} (black solid line) is ~10% different compared to ~30% different between MODIS and MOBY b_{bp} (black dotted line) for the peak b_{bp} difference between sensors (which occurs around May – August). These differences are largely because CALIOP b_{bp} exceeds MOBY b_{bp} (Figure 4b). Overall, the observed seasonal bias between MODIS and MOBY at this local site is consistent with the seasonal bias between MODIS and CALIOP on global scales. MODIS b_{bp} greatly exceeds MOBY b_{bp} during the summer months compared to the winter months in the Northern Hemisphere.

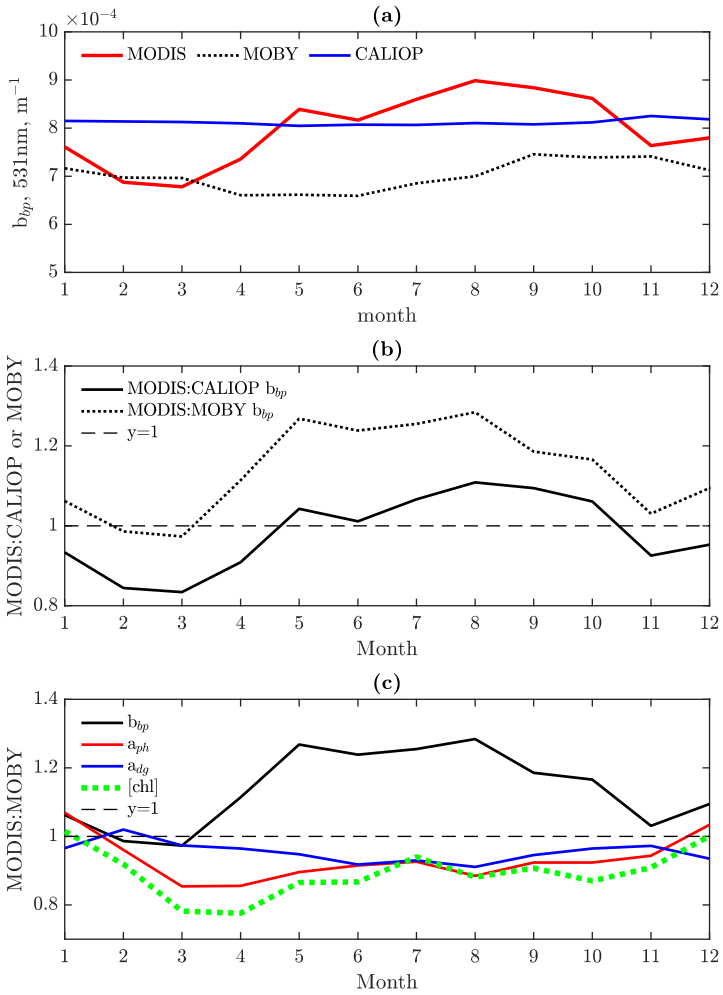

Figure 4. Comparison of MODIS with CALIOP b_{bp} and MOBY products at the MOBY site. a) monthly averaged MODIS (red), MOBY (black dashed line), and CALIOP (blue) b_{bp}. b) MODIS:CALIOP (black solid line) and MODIS:MOBY (black dotted line) b_{bp} at 531 nm. Dashed line indicates a ratio of 1. c) MODIS: MOBY b_{bp} (531 nm, black line), MODIS: MOBY a_{ph} (443 nm, red line), MODIS: Moby a_{dg} (412 nm, blue line), MODIS: MOBY chlorophyll, green dashed line.

MOBY and MODIS R_{rs} are converted into other attributes besides b_{bp}, including phytoplankton absorption (443 nm, a_{ph}, red line in Figure 4c), absorption from dissolved detrital organic matter (412nm, $a_{dg,}$ blue line in Figure 4c), and chlorophyll (chl, green dashed line in

Figure 4c). In contrast to MOBY and MODIS b_{bp}, all of the absorbing constituents derived from MODIS R_{rs} are lower on average compared to MOBY. Of all attributes, the difference between b_{bp} exhibits the greatest dissimilarity between sensors, with differences up to 30%. However, differences in chlorophyll between the two sensors can reach 20% from March to April. Both a_{dg} (412) and a_{ph} (443) are affected by a seasonal bias in R_{rs}, but to a lesser extent and with differences between MOBY and MODIS a_{dg} and a_{ph} not exceeding 15% throughout the annual cycle.

3.4 Multivariate regression analysis findings

Results from the multivariate regression analysis (Figure 5) indicate a significant dependence on the solar and sensor zenith angle at almost all wavelengths, as well as on BRDF slope (β) across wavelengths. A β close to 0 indicates no correspondence with $Rrs_{¿}$, while a negative β indicates an inverse relationship. Ideally, the β_0, slope between $Rrs_{¿}$ and Rrs_{moby} should be 1, while the slope for other independent variables should be 0 (indicating independence between the variables and the *Rrs* matchups). A deviation in β from 0 indicates a residual bias in the matchups due to improper correction to these parameters on their relationship with $Rrs_{¿}$.

At longer wavelengths, slopes for the optical depth and the angstrom coefficient increase. At wavelengths 412 and 443 nm, other than the zenith angles, the BRDF correction factor has the largest slope relative to the other parameters, indicating that the BRDF correction has the most co-linearity with the R_{rs} matchups. This BRDF slope decreases for longer wavelengths and the slope of the Angstrom coefficient and the optical depth is more pronounced. Overall, the BRDF

factor slope showed a consistent and statistically significant departure from the zero line. However, the aerosol correction also plays a factor.

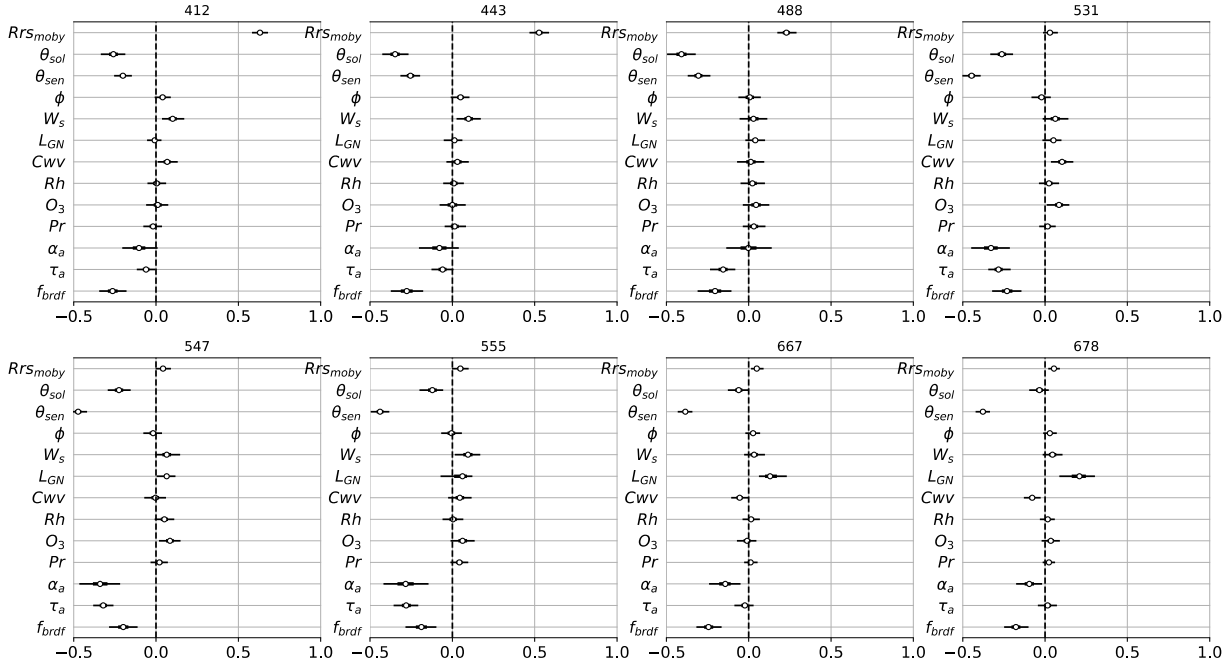

Figure 5: Forest plot of the MLR slope coefficients for wavelengths 412, 443, 488, 531, 547, 555, 667, and 678 nm. The y-axis shows the β coefficients for each explanatory variable and the x-axis shows the scale of these coefficients. The open circle represents the mode of the posterior, while the error bar represents the 94% high density interval of the distribution.

4.0 Discussion

On global, regional, and local scales, we have found seasonal variability in ocean color R_{rs} that stands in contrast to observations from CALIOP, Argo, and MOBY. In many locations, observations from ocean color R_{rs} (relative to the assets listed above) are roughly symmetrical over the annual cycle, making it difficult to reconcile these observations with known seasonal progressions in phytoplankton populations [which tend to be asymmetric with respect to the

seasonal cycle (e.g., Behrenfeld et al., 2013; Siegel et al., 2002)]. Seasonal symmetry is, however, expected in products directly dependent on solar geometry (including daylength, which is directly proportional to solar zenith angle). Therefore, the observed shape in R_{rs} over the annual cycle strongly implies that the seasonal bias is not related to in-water processes and instead reflects an artifact stemming from processing. In this study we have eliminated many potential candidates causing the seasonal bias, but we have not yet identified the specific issue. Nevertheless, we can still examine the extent to which the bias is problematic for different regions and times. Here, we reflect on what is learned from cross-comparing observational platforms to discover the widespread seasonal bias in satellite ocean color observations.

4.1 Importance of additional assets to improve remote sensing

In this study, we used CALIOP, MOBY, and Argo observations of b_{bp} to primarily assess MODIS observations over an annual cycle from local to global scales. Without CALIOP data, we would not have identified the seasonal bias in ocean color observations and without CALIOP data there would be no way to quantify and describe the extent of the seasonal bias in b_{bp} worldwide. Without MOBY data, there would be no way to confirm that the bias is present in R_{rs} and not just products derived from R_{rs}. We also learn from MOBY that b_{bp} is most strongly affected by the R_{rs} bias in comparison to chlorophyll, phytoplankton absorption, and dissolved organic matter absorption. Without Argo data, it would not have been possible to test the accuracy of MODIS and CALIOP on regional scales and, ultimately, to learn that CALIOP observations better describe the seasonal cycle in b_{bp} compared to ocean color. Thus, the importance of using additional assets to validate, improve, and assess uncertainties in remote sensing and its products cannot be overstated. For decades, a seasonal bias in ocean color

observations has existed but remained unknown. Only through the recent deployment of Argo floats equipped with backscattering sensors and recent retrieval developments to produce CALIOP b_{bp} could the seasonal bias in R_{rs} from ocean color satellites be identified and described.

Closure in b_{bp} has not been reached between passive remote sensing, in situ sampling, and active remote sensing. We note that none of these platforms observe true b_{bp}, as these sensors observe scattering at different viewing angles and are measuring only a portion of the volume scattering function. Although we cannot say exactly what causes the seasonal bias in MODIS R_{rs}, we speculate that the reason CALIOP is not similarly biased is because lidar is a more direct measurement of b_{bp} compared to ocean color, is not affected by sun zenith angle, and is less affected by the overlying atmosphere (including clouds, e.g., Hostetler et al., 2018 and references therein). Ocean color R_{rs} is the signal remaining after removing surface glint, white-caps, atmospheric molecular and aerosol effects, and following BRDF correction. In addition, deriving b_{bp} from R_{rs} requires spectral assumptions regarding scattering and absorbing constituents in seawater.

While satellite ocean color observations are undoubtedly biased on seasonal scales, both satellite ocean color and satellite lidar observations exhibit an overall biased in lower biomass areas. Argo b_{bp} observations in oligotrophic regions (South Pacific, South Atlantic, Indian ocean gyres) are roughly 30% lower than CALIOP and up to 50% lower than MODIS. Previous work confirms this finding, as Bisson et al. (2021) found good correspondence between Argo, MODIS, and CALIOP for $b_{bp} > 0.001$ m^{-1}, but not for $b_{bp} < 0.001$ m^{-1} (700 nm). The reason for the elevated MODIS and CALIOP b_{bp} in these regions is also not fully understood.

4.2 What can we learn about R_{rs} from diagnosing the seasonal bias?

In this study, we employed a series of diagnostic tests in an attempt to identify any underlying cause of the seasonal bias in satellite ocean color b_{bp}. Despite testing ideas thought to have a large influence on b_{bp} (such as Raman correction, assumed spectral shape of absorption and backscattering), we found that specific assumptions in R_{rs} inversions had little influence on the seasonal bias in b_{bp}. Put simply, atmospheric correction schemes have a larger effect on R_{rs}-derived products than the models used to derive those products.

The bias in R_{rs} is worse for longer wavelengths. Even though R_{rs} at 667 nm has relatively small signal overall, it influences b_{bp} and chlorophyll substantially. For example, a seasonal bias at MOBY was not pronounced at lower wavelengths of R_{rs}, even though there existed a clear seasonal bias in b_{bp} derived from R_{rs} at MOBY due to the strong bias of R_{rs} (667 nm). One reason for the MOBY bias at 667 nm could be that surface MOBY measurements are extrapolated from observations > 1m depth and errors in this extrapolation can approach 80% at longer wavelengths (e.g., 650 nm, see Figure 7 of Li et al., 2016). Future inversion algorithms should consider adding weights by wavelength in the cost function (proportional to their uncertainty), which would give higher importance to R_{rs} at lower wavelengths (Werdell et al., 2018).

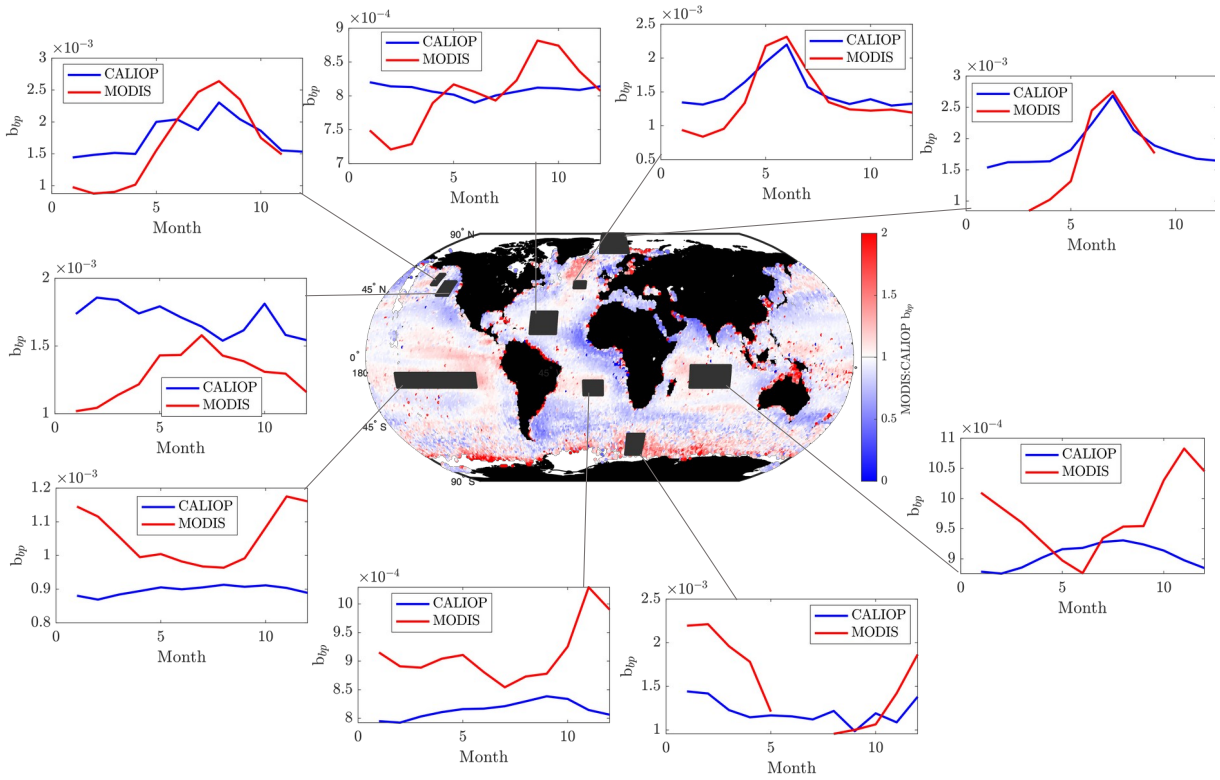

Figure 6. Global comparisons of backscattering derived from MODIS and CALIOP

4.3 Global implications of R_{rs} bias

Although the bulk of our analysis focused on the MODIS sensor, the seasonal bias in satellite R_{rs} is present in SeaWiFS and VIIRS imagery as well. Findings from studies that rely on seasonal analyses from any of these three sensors may thus need revisiting, especially if b_{bp} or chlorophyll were used. Places particularly affected by the seasonal bias are the low biomass areas (Figure 6), including Bermuda and the North Pacific, which are sites of long-term time series field observations (Steinberg et al., 2001, Freeland, 2007). Low biomass regions are also affected for the months in which MODIS provides observations (Figure 6, bottom right panel). Areas with a large biological signal are not obviously affected to a substantial degree, including the North Atlantic, Arctic Ocean, and Gulf of Alaska.

494 Ultimately, the seasonal bias in satellite ocean color observations yields a seasonal signal in
495 many regions that is inaccurate. Accurate seasonal measurements of b_{bp} in particular are needed
496 to characterize temporal dynamics of phytoplankton carbon (Graff et al., 2015) and particulate
497 organic carbon. Phytoplankton carbon observations from satellites are used in many models,
498 from net primary production to carbon export. Net primary production algorithms require growth
499 rates calculated from phytoplankton physiological states, commonly assessed using satellite
500 Chl:Carbon ratios (Behrenfeld et al., 2005). Mechanistic carbon export models that use food-web
501 interactions rely entirely on the derivative of phytoplankton carbon over the annual cycle in order
502 to diagnose grazing rates and assess other loss terms (Siegel et al., 2014, Bisson et al., 2020).
503 Using seasonally biased phytoplankton carbon from ocean color will thus likely affect
504 quantification of carbon flux and net primary productivity in lower biomass areas.
505 Phytoplankton size is another area where accurate b_{bp} observations are especially needed over
506 the seasonal cycle. One particle size algorithm (Kostadinov et al., 2010) uses b_{bp} observations to
507 track changes in particle size distributions from month to month. This algorithm has been used
508 widely in ecological and carbon cycle studies. A recent carbon export study found that including
509 particle size in ecological models improved the performance of those models (Bisson et al.,
510 2020), but an incorrect seasonal cycle of particle size will introduce bias into the modeled
511 results. Introducing seasonal error into carbon cycle models may create a particularly significant
512 issue for oligotrophic areas dominated by picophytoplankton, which have been getting more
513 attention for their role in carbon export (Richardson and Jackson, 2007, Richardson, 2019 and
514 refs therein). Oligotrophic regions may also be growing in areal extent due to climate change
515 and they are predicted to continue growing in future years (Irwin and Oliver, 2009), making
516 them a substantial element of the global ocean system. If an artificial seasonality in

phytoplankton size is introduced by algorithms built from ocean color b_{bp}, it will be difficult to predict the ecological fate of oligotrophic regions.

Finally, the observed seasonal bias in chlorophyll from ocean color is problematic because chlorophyll is commonly used for assessing phytoplankton physiology and growth rate. Accurate determinations of phytoplankton growth rate are needed to produce accurate net primary production seasonal cycles. Chlorophyll is also commonly used to discriminate diatoms and phytoplankton functional types (Uitz et al., 2010, Soppa et al., 2014, Hirata et al., 2011). Given that our findings suggest chlorophyll seasonal biases of up to 20% (and perhaps more at locations other than MOBY), chlorophyll-based algorithms for phytoplankton functional types should be used with caution. Artificial seasonality in satellite chlorophyll may wrongly prescribe shifting phytoplankton communities within these empirically-derived models. A slightly better approach may come from using absorption spectra to characterize phytoplankton rather than chlorophyll (Chase et al., 2017) because phytoplankton absorption appears to be less affected by the R_{rs} bias. In all cases, the uncertainty due to the seasonal bias as described here should be quantified.

4.4 Recommendations

At present, the remaining top candidates for the source of the seasonal bias in $R_{rs,}$ which are shown to depend on angular geometry, are 1) instrument calibration, 2) atmospheric correction, 3) modeling of the water signal, and 4) vicarious calibration. The instrument calibration could introduce a bias into R_{rs} due to scan angle dependence, polarization correction (which is a strong function of scattering angle), and other non-linear effects, such as a temperature dependence, and significantly affect the determination of aerosol properties.

Atmospheric correction removes the perturbing signal arising from molecular and aerosol scattering (as well as absorption) and it also accounts for gaseous absorption (e.g., by ozone) and ocean surface effects (e.g., glint and whitecaps). Some of these effects are not well-known or determined with sufficient accuracy, yielding angular-dependent R_{rs} errors. The retrieved signal from the water body, as viewed from space, needs to be corrected for diffuse atmospheric transmittance and normalized to yield R_{rs} in a reference geometry. This requires proper modeling of bidirectional effects and interactions between the water body and the atmosphere. The current treatment could be improved by choosing a different BRDF (e.g., Park and Ruddick, 2005), taking into account the water-leaving signal backscattered by the atmosphere (Tanré et al., 1979), including anisotropy of the sub-surface upwelling light field in the diffuse transmittance (Yang and Gordon, 1997), and incorporating Earth sphericity (Frouin et al., 2019; Ramon et al., 2019). The vicarious calibration process aims to reduce the average temporal systematic bias for in situ and satellite observations at MOBY, but vicarious calibration does not address seasonal bias issues due to the instrument or the atmospheric correction. For vicarious calibration to be effective, the modeled atmospheric contribution needs to be accurate.

We note that our multivariate regression analysis found that slopes of the angstrom coefficient and aerosol optical depth were more pronounced at mid visible wavelengths, but less at shorter wavelengths. Typically, the choice of aerosol model, presented as the angstrom coefficient, affects shorter wavelengths moreso than longer ones, due to the atmospheric correction assumptions of extrapolating the aerosol spectral dependence from the near-infrared wavelengths. However, the slopes representing the BRDF were more pronounced at 412 and 443 nm than the aerosols' effect, suggesting a more complex underlying process that perhaps combine the effects of the BRDF and the aerosols correction, or more unknown parameters. The

dynamic range of the ocean and the aerosol signals also plays a role since the dynamic range of the R_{rs} can be orders of magnitude different from the blue end of the spectrum to the red end. Future work should explore different aerosol models and consider integrating CALIOP-derived aerosol optical depth information along with MODIS data (as in Kim et al., 2013, which showed substantial differences between CALOP and MODIS optical depth).

Until a solution to the seasonal bias is identified and implemented, we recommend using CALIOP b_{bp} data for global scale when possible. Although the focus of this manuscript has been on the seasonal bias in ocean color R_{rs}, we have previously found annually averaged regional differences in phytoplankton carbon from MODIS compared to CALIOP of up to 50% (Bisson et al., 2021), especially in low biomass regions affected the seasonal bias. For this reason, studies should acknowledge the seasonal bias when interpreting spatiotemporal patterns in ocean color data. Despite CALIOP's ~100m footprint and the fact that it does not provide the comparable spatial coverage as SeaWiFS, MODIS, and VIIRS, data from CALIOP can be averaged into the 1-degree monthly bins that are a common spatiotemporal resolution of models. We also recommend using models that discriminate phytoplankton types and size with caution due to the revealed uncertainty in their input products (i.e., ocean color $b_{bp,}$ $R_{rs,}$ and/or a_{ph}).

5 Conclusion

In this study we provide evidence for a global seasonal bias in satellite ocean color observations. Our findings can be summarized by the following points:

- Independent global observations are critical to validate remote sensing products.

- The entire record of satellite ocean color over the last few decades is likely significantly seasonally biased in low biomass regions.
- Particulate backscattering and chlorophyll are most affected by a seasonal bias in R_{rs}, while phytoplankton and dissolved detrital absorption are less affected.
- The seasonal bias in R_{rs} is most pronounced at longer wavelengths (i.e., 667 nm).
- Community efforts should help identify the root source of the problem, as all past, present, and future data (from the PACE mission, for example) will be affected until a solution can be implemented.

References

Behrenfeld, M. J., Doney, S. C., Lima, I., Boss, E. S., & Siegel, D. A. (2013). Annual cycles of ecological disturbance and recovery underlying the subarctic Atlantic spring plankton bloom. *Global biogeochemical cycles*, *27*(2), 526-540.

Behrenfeld, M. J., O'Malley, R. T., Boss, E. S., Westberry, T. K., Graff, J. R., Halsey, K. H., ... & Brown, M. B. (2016). Revaluating ocean warming impacts on global phytoplankton. *Nature Climate Change*, *6*(3), 323-330.

Behrenfeld, M. J., Hu, Y., Hostetler, C. A., Dall'Olmo, G., Rodier, S. D., Hair, J. W., & Trepte, C. R. (2013). Space−based lidar measurements of global ocean carbon stocks. *Geophysical Research Letters*, *40*(16), 4355-4360.

607 Behrenfeld, M. J., Westberry, T. K., Boss, E. S., O'Malley, R. T., Siegel, D. A., Wiggert, J. D., ...
608 & Moore, J. K. (2009). Satellite-detected fluorescence reveals global physiology of ocean
609 phytoplankton. *Biogeosciences*, *6*(5), 779.
610
611 Behrenfeld, M. J., & Falkowski, P. G. (1997). Photosynthetic rates derived from satellite−based
612 chlorophyll concentration. *Limnology and oceanography*, *42*(1), 1-20.
613
614 Behrenfeld, M. J., Boss, E., Siegel, D. A., & Shea, D. M. (2005). Carbon−based ocean
615 productivity and phytoplankton physiology from space. *Global biogeochemical cycles*, *19*(1).
616 Bisson, K. M., Boss, E., Westberry, T. K., & Behrenfeld, M. J. (2019). Evaluating satellite
617 estimates of particulate backscatter in the global open ocean using autonomous profiling
618 floats. *Optics express*, *27*(21), 30191-30203.
619
620 Bisson, K., Siegel, D. A., & DeVries, T. (2020). Diagnosing mechanisms of ocean carbon export
621 in a satellite-based food web model. *Frontiers in Marine Science*.
622
623 Bisson, K. M., Boss, E., Westberry, T. K., & Behrenfeld, M. J. (2019). Evaluating satellite
624 estimates of particulate backscatter in the global open ocean using autonomous profiling
625 floats. *Optics express*, *27*(21), 30191-30203.
626
627 Bracher, A., Vountas, M., Dinter, T., Burrows, J. P., Röttgers, R., & Peeken, I. (2009).
628 Quantitative observation of cyanobacteria and diatoms from space using PhytoDOAS on
629 SCIAMACHY data. *Biogeosciences*, *6*, 751-764.

Chase, A. P., Boss, E., Cetinić, I., & Slade, W. (2017). Estimation of phytoplankton accessory pigments from hyperspectral reflectance spectra: toward a global algorithm. *Journal of Geophysical Research: Oceans*, *122*(12), 9725-9743.

Clark, D. K., Yarbrough, M. A., Feinholz, M., Flora, S., Broenkow, W., Kim, Y. S., ... & Mueller, J. L. (2003). MOBY, a radiometric buoy for performance monitoring and vicarious calibration of satellite ocean color sensors: Measurement and data analysis protocols. Chapter 2.

Dierssen, H., McManus, G. B., Chlus, A., Qiu, D., Gao, B. C., & Lin, S. (2015). Space station image captures a red tide ciliate bloom at high spectral and spatial resolution. *Proceedings of the National Academy of Sciences*, *112*(48), 14783-14787.

Dutkiewicz, S., Hickman, A. E., Jahn, O., Henson, S., Beaulieu, C., & Monier, E. (2019). Ocean colour signature of climate change. *Nature communications*, *10*(1), 1-13.

Dutkiewicz, S. (2020). Synergy between Ocean Colour and Biogeochemical/Ecosystem Models. *IOCCG Report Series, No. 19, International Ocean Colour Coordinating Group, Dartmouth, Canada.* http://dx.doi.org/10.25607/OBP-711.

Evers-King, H., Martinez-Vicente, V., Brewin, R. J., Dall'Olmo, G., Hickman, A. E., Jackson, T., ... & Roy, S. (2017). Validation and intercomparison of ocean color algorithms for estimating particulate organic carbon in the oceans. *Frontiers in Marine Science*, *4*, 251.

Gordon, H. R., Brown, O. B., Evans, R. H., Brown, J. W., Smith, R. C., Baker, K. S., & Clark, D. K. (1988). A semianalytic radiance model of ocean color. *Journal of Geophysical Research: Atmospheres*, *93*(D9), 10909-10924.

Freeland, H. (2007). A short history of Ocean Station Papa and Line P. *Progress in Oceanography*, *75*(2), 120-125.

Graff, J. R., Westberry, T. K., Milligan, A. J., Brown, M. B., Dall'Olmo, G., van Dongen-Vogels, V., ... & Behrenfeld, M. J. (2015). Analytical phytoplankton carbon measurements spanning diverse ecosystems. *Deep Sea Research Part I: Oceanographic Research Papers*, *102*, 16-25.

Hirata, T., Aiken, J., Hardman-Mountford, N., Smyth, T. J., & Barlow, R. G. (2008). An absorption model to determine phytoplankton size classes from satellite ocean colour. *Remote Sensing of Environment*, *112*(6), 3153-3159.

Henson, S. A., Sarmiento, J. L., Dunne, J. P., Bopp, L., Lima, I., Doney, S. C., ... & Beaulieu, C. (2010). Detection of anthropogenic climate change in satellite records of ocean chlorophyll and productivity. *Biogeosciences*, *7*(2), 621-640.

Hirata, T., Hardman-Mountford, N. J., Brewin, R. J. W., Aiken, J., Barlow, R., Suzuki, K., ... & Yamanaka, Y. (2011). Synoptic relationships between surface Chlorophyll-a and diagnostic pigments specific to phytoplankton functional types. *Biogeosciences*, *8*(2), 311-327.

Hoge, F. E., & Lyon, P. E. (2002). Satellite observation of chromophoric dissolved organic matter (CDOM) variability in the wake of hurricanes and typhoons. *Geophysical Research Letters*, *29*(19), 14-1.

Hostetler, C. A., Behrenfeld, M. J., Hu, Y., Hair, J. W., & Schulien, J. A. (2018). Spaceborne lidar in the study of marine systems. *Annual review of marine science*, *10*, 121-147.

Irwin, A. J., & Oliver, M. J. (2009). Are ocean deserts getting larger?. *Geophysical Research Letters*, *36*(18).

Kim, M. H., Kim, S. W., Yoon, S. C., & Omar, A. H. 2013. Comparison of aerosol optical depth between CALIOP and MODIS−Aqua for CALIOP aerosol subtypes over the ocean. J. Geophys. Res.: Atmospheres, 118(23), 13-241.

Kramer, S. J., Roesler, C. S., & Sosik, H. M. (2018). Bio-optical discrimination of diatoms from other phytoplankton in the surface ocean: Evaluation and refinement of a model for the Northwest Atlantic. *Remote sensing of environment*, *217*, 126-143.

Kostadinov, T. S., Siegel, D. A., & Maritorena, S. (2010). Global variability of phytoplankton functional types from space: assessment via the particle size distribution. *Biogeosciences Discussions*, *7*(3).

699 Lange, P. K., Werdell, P. J., Erickson, Z., Dall'Olmo, G. I. O. R. G. I. O., Brewin, R. J., Zubkov,
700 M. V., ... & Poulton, N. (2020). Radiometric approach for the detection of picophytoplankton
701 assemblages across oceanic fronts. *Optics Express*, 1-23.
702
703 Lee, Z., Carder, K. L., & Arnone, R. A. (2002). Deriving inherent optical properties from water
704 color: a multiband quasi-analytical algorithm for optically deep waters. *Applied optics*, *41*(27),
705 5755-5772.
706
707 Lee, Z., Hu, C., Shang, S., Du, K., Lewis, M., Arnone, R., & Brewin, R. (2013). Penetration of
708 UV−visible solar radiation in the global oceans: Insights from ocean color remote
709 sensing. *Journal of Geophysical Research: Oceans*, *118*(9), 4241-4255.
710
711 Li, L., Stramski, D., & Reynolds, R. A. (2016). Effects of inelastic radiative processes on the
712 determination of water-leaving spectral radiance from extrapolation of underwater near-surface
713 measurements. *Applied Optics*, *55*(25), 7050-7067.
714
715 Loisel, H., Nicolas, J. M., Sciandra, A., Stramski, D., & Poteau, A. (2006). Spectral dependency
716 of optical backscattering by marine particles from satellite remote sensing of the global ocean.
717 *Journal of Geophysical Research: Oceans*, *111*(C9).
718 Matsuoka, A., Boss, E., Babin, M., Karp-Boss, L., Hafez, M., Chekalyuk, A., ... & Bricaud, A.
719 (2017). Pan-Arctic optical characteristics of colored dissolved organic matter: Tracing dissolved
720 organic carbon in changing Arctic waters using satellite ocean color data. *Remote Sensing of*
721 *Environment*, *200*, 89-101.

Maritorena, S., Siegel, D. A., & Peterson, A. R. (2002). Optimization of a semianalytical ocean color model for global-scale applications. *Applied optics*, *41*(15), 2705-2714.

Richardson, T. L., & Jackson, G. A. (2007). Small phytoplankton and carbon export from the surface ocean. *Science*, *315*(5813), 838-840.

Richardson, T. L. (2019). Mechanisms and pathways of small-phytoplankton export from the surface ocean. *Annual Review of Marine Science*, *11*, 57-74.

Salvatier, J., Wiecki, T.V. and Fonnesbeck, C., 2016. Probabilistic programming in Python using PyMC3. *PeerJ Computer Science*, *2*, p.e55.

Sathyendranath, S., Aiken, J., Alvain, S., Barlow, R., Bouman, H., Bracher, A., ... & Clementson, L. A. (2014). Phytoplankton functional types from Space. In *(Reports of the International Ocean-Colour Coordinating Group (IOCCG); 15)* (pp. 1-156). International Ocean-Colour Coordinating Group.

Siegel, D. A., Doney, S. C., & Yoder, J. A. (2002). The North Atlantic spring phytoplankton bloom and Sverdrup's critical depth hypothesis. *science*, *296*(5568), 730-733.

743 Siegel, D. A., O'Brien, M. C., Garver, S. A., Brody, E. A., Sorensen, J. C., Michaels, A. F., ... &
744 Nelson, N. B. (1997, February). Bermuda bio-optics project (BBOP). In *Ocean Optics XIII* (Vol.
745 2963, pp. 308-313). International Society for Optics and Photonics.
746
747 Siegel, D. A., Buesseler, K. O., Behrenfeld, M. J., Benitez-Nelson, C. R., Boss, E., Brzezinski,
748 M. A., ... & Perry, M. J. (2016). Prediction of the export and fate of global ocean net primary
749 production: The EXPORTS science plan. *Frontiers in Marine Science*, *3*, 22.
750
751 Siegel, D. A., Buesseler, K. O., Doney, S. C., Sailley, S. F., Behrenfeld, M. J., & Boyd, P. W.
752 (2014). Global assessment of ocean carbon export by combining satellite observations and food‐
753 web models. *Global Biogeochemical Cycles*, *28*(3), 181-196.
754
755 Soppa, M. A., Hirata, T., Silva, B., Dinter, T., Peeken, I., Wiegmann, S., & Bracher, A. (2014).
756 Global retrieval of diatom abundance based on phytoplankton pigments and satellite
757 data. *Remote Sensing*, *6*(10), 10089-10106.
758
759 Steinberg, D. K., Carlson, C. A., Bates, N. R., Johnson, R. J., Michaels, A. F., & Knap, A. H.
760 (2001). Overview of the US JGOFS Bermuda Atlantic Time-series Study (BATS): a decade-
761 scale look at ocean biology and biogeochemistry. *Deep Sea Research Part II: Topical Studies in*
762 *Oceanography*, *48*(8-9), 1405-1447.
763
764 Stramski, D., Reynolds, R. A., Kahru, M., & Mitchell, B. G. (1999). Estimation of particulate
765 organic carbon in the ocean from satellite remote sensing. *Science*, *285*(5425), 239-242.

Stumpf, R. P. (2001). Applications of satellite ocean color sensors for monitoring and predicting harmful algal blooms. *Human and Ecological Risk Assessment: An International Journal*, *7*(5), 1363-1368.

Stumpf, R. P. (1988). Sediment transport in Chesapeake Bay during floods: analysis using satellite and surface observations. *Journal of Coastal Research*, 1-15.

Tao, J., & Hill, P. S. (2019). Correlation of Remotely Sensed Surface Reflectance With Forcing Variables in Six Different Estuaries. *Journal of Geophysical Research: Oceans*, *124*(12), 9439-9461.

Uitz, J., Claustre, H., Gentili, B., & Stramski, D. (2010). Phytoplankton class−specific primary production in the world's oceans: Seasonal and interannual variability from satellite observations. *Global Biogeochemical Cycles*, *24*(3).

Wei, G., Tang, D., & Wang, S. (2008). Distribution of chlorophyll and harmful algal blooms (HABs): A review on space based studies in the coastal environments of Chinese marginal seas. *Advances in Space Research*, *41*(1), 12-19.

Werdell, P. J., Behrenfeld, M. J., Bontempi, P. S., Boss, E., Cairns, B., Davis, G. T., ... & Knobelspiesse, K. D. (2019). The Plankton, Aerosol, Cloud, ocean Ecosystem mission: status, science, advances. *Bulletin of the American Meteorological Society*, *100*(9), 1775-1794.

Westberry, T., Behrenfeld, M. J., Siegel, D. A., & Boss, E. (2008). Carbon−based primary productivity modeling with vertically resolved photoacclimation. *Global Biogeochemical Cycles*, *22*(2).

Westberry, T. K., & Siegel, D. A. (2006). Spatial and temporal distribution of Trichodesmium blooms in the world's oceans. *Global Biogeochemical Cycles*, *20*(4).

Westberry, T. K., Boss, E., & Lee, Z. (2013). Influence of Raman scattering on ocean color inversion models. *Applied optics*, *52*(22), 5552-5561.

Yu, X., Lee, Z., Shen, F., Wang, M., Wei, J., Jiang, L., & Shang, Z. (2019). An empirical algorithm to seamlessly retrieve the concentration of suspended particulate matter from water color across ocean to turbid river mouths. *Remote Sensing of Environment*, *235*, 111491.

Supplementary Figure Captions

Supplementary Figure 1. Monthly climatologies constructed from exact daily matchups between MODIS and CALIOP (written as 'lidar') b_{bp}, binned to 9km. (a) Results for 531 nm. (b) Results for 443 nm. The Lee et al., 2013 Raman scattering correction scheme was applied to MODIS reflectances. (c) Daily maps of MODIS and CALIOP data showing a gap in the western pacific where there is no coincident overlap.

Supplementary Figure 2. (a) Monthly climatologies of MODIS: CALIOP constructed from average monthly values of MODIS and CALIOP data, both at 1-degree bins. MODIS R_{rs} is corrected for Raman scattering using the Westberry et al., 2013 algorithm. (b) Monthly averages of the percent difference in MODIS b_{bp} (531 nm) using the Westberry et al., 2013 algorithm relative to the Lee et al., 2013 algorithm for Raman scattering correction. (c) Monthly climatologies constructed from exact daily matchups between MODIS and CALIOP (written as 'lidar') b_{bp} (555 nm), binned to 9km. No Raman scattering correction was applied.

Supplementary Figure 3, (a) Monthly climatologies of MODIS: CALIOP b_{bp} constructed from exact daily matchups between MODIS and CALIOP (written as 'lidar') b_{bp}, binned to 9km, where the 'QAA' algorithm for CDOM absorption was used to derive MODIS b_{bp}. (b) Same as 3a except that the GSM algorithm (a single value that is constant everywhere) was used for b_{bp} slope compared to the spatially variant QAA algorithm used in all other figures. (c) Same as 3a except that the 'Ciotti and Bricaud, 2006' algorithm was used for phytoplankton absorption compared to the Bricaud 1998 algorithm that is typically used.

Supplementary Figure 4. (a). Monthly climatologies of MODIS: CALIOP constructed from exact daily matchups between MODIS and CALIOP (written as 'lidar') b_{bp}, binned to 9km. (b) monthly climatologies of MODIS: CALIOP constructed from monthly average values of MODIS and CALIOP b_{bp}, binned to 1-degree.

Supplementary Figure 5. Daily matchups between CALIOP b_{bp} and passive ocean color b_{bp}, binned to 9km. (a) MODIS: CALIOP ratios throughout the annual cycle (over the period 2006 –

2017, the overlapping range), (b) SeaWiFs:CALIOP ratios throughout the annual cycle (from 2006-2010, the overlapping range), (c) VIIRS:CALIOP ratios throughout the annual cycle (2006 – 2017, the overlapping range).

Supplementary Figure 6. Comparison of MODIS Level-2 data with CALIOP b_{bp} and Argo b_{bp} in the South Atlantic (15-21S, 10-35W). Note that MODIS and CALIOP are for 2010, while Argo data are monthly averages for 2016 to the present (due to insufficient data within any given year). (a) $b_{bp,}$ 531 nm. (b) Ratio of MODIS:CALIOP b_{bp} over the annual cycle of 2010. (c) Photosynthetically Active Radiation (PAR) and solar zenith angle. (d) R_{rs} ratios (Raman corrected and not Raman corrected). (e) Aerosol optical thickness. (f) Angstrom parameter.

Supplementary Figure 7. Comparison of MODIS Level-2 data with CALIOP b_{bp} and Argo b_{bp} in the Indian Ocean (10-25S, 55-95E). Note that MODIS and CALIOP are for 2010, while Argo data are monthly averages for 2016 to the present (due to insufficient data within any given year). (a) $b_{bp,}$ 531 nm. (b) Ratio of MODIS:CALIOP b_{bp} over the annual cycle of 2010. (c) Photosynthetically Active Radiation (PAR) and solar zenith angle. (d) R_{rs} ratios (Raman corrected and not Raman corrected). (e) Aerosol optical thickness. (f) Angstrom parameter.